# CHAPTER 2

## Material and Methods

## 2.1 Introduction

The chapter describes the standard experimental protocols used in this thesis to synthesize iron oxide-based p-n heterojunction nanocomposites. It also gives the methodology for the determination of the catalytic performance of synthesized nanomaterials for different applications. Finally, the chapter explains the working principles of instruments utilized in this thesis.

## 2.2 Chemicals

In this thesis, analytical grade chemicals were used without further purification. All investigations were conducted with double-distilled water of ~ 6.8 pH. Table 2.1 displays the particulars of the chemicals used in experimental studies.

**Table 2.1** Names, chemical formula, molecular weights, manufacturer's name, and physical appearances of the reagents used.

| Sr. No. | Chemical Name | Chemical formula | Molecular weight (g) | Manufacturer | Appearance |
|---|---|---|---|---|---|
| 1 | Iron (II) sulfate heptahydrate | $FeSO_4.7H_2O$ | 278.02 | Merck | Blue-green Crystal |
| 2 | Iron (III) Chloride | $FeCl_3$ | 168.20 | Merck | Brownish-black crystal |
| 3 | Starch | $(C_6H_{10}O_5)_n$ | | Merck | White Powder |
| 4 | Silver nitrate | $AgNO_3$ | 169.87 | Merk | White crystal |
| 5 | Copper nitrate | $Cu(NO_3)_2.3H_2O$ | 241.60 | Merk | Blue Crystal |
| 6 | Sodium hydroxide | NaOH | 40 | Merck | White Pellet |
| 7 | Hydrogen peroxide | $H_2O_2$ | 34.01 | Merck | Colorless liquid |
| 8 | p-nitrophenol | $C_6H_5NO_3$ | 139.11 | Spectrochem | Yellow Solid |
| 9 | Methyl orange | $C_{14}H_{14}N_3NaO_3S$ | 327.33 | Molychem | Orange powder |

## 2.3 Synthesis of iron oxide-based p-n heterojunction photocatalysts

### 2.3.1 Synthesis of starch functionalized $Fe_3O_4/Ag/Ag_2O$ nanostructures

Analytical grade $FeSO_4.7H_2O$ (Merck), NaOH (Merck), water-soluble starch (Merck), and $AgNO_3$ (Merck) were used for the synthesis of $Fe_3O_4/Ag/Ag_2O$ nanostructure. Stepwise, co-precipitation methodologies were used to synthesize starch functionalized $Fe_3O_4/Ag/Ag_2O$ heterojunction photocatalyst. Firstly, starch functionalized $Fe_3O_4$ nanoparticle was prepared by co-precipitation [Singh *et al*. 2016]. An aqueous solution of 0.2 M $FeSO_4.7H_2O$ and 2wt% starch was mixed and added dropwise into a previously heated 0.4 M NaOH solution at 80°C. A dark black precipitate appeared on completion of the addition. The reaction mixture was further heated at 80°C for two more hours to ensure complete precipitation. The resultant precipitate was separated by magnetic decantation, repeatedly washed with double distilled water and alcohol, and then dried at 40°C in a hot air oven. The symbol SMNPs denotes the resulting powder sample.

Nanocomposite samples (starch functionalized $Fe_3O_4/Ag/Ag_2O$ composites) were prepared by re-dispersing a certain amount of the dried powder of SMNPs sample in double distilled water then mixing it with an appropriate volume of the $AgNO_3$ aqueous solution. The reaction mixture was then kept in a thermostatic water bath (for 24 hours at 35°C) for adsorbing $Ag^+$ ions on the surface of SMNPs. This suspension was then added in a dropwise manner to aqueous NaOH with constant heating and stirring at 60 °C. For complete precipitation, the reaction mixture was heated at 60 °C with stirring for two more hours. The prepared nanocomposite precipitate was magnetically separated and washed several times with distilled water until the washings turned neutral. Two nanocomposites, sample C1 and C2, were prepared by varying the $AgNO_3$ concentration. The nanocomposite C1 was fabricated with 0.01M $AgNO_3$ while C2 with 0.02 M $AgNO_3$.

### 2.3.2 Synthesis of starch functionalized $Fe_3O_4/Cu_2O$ nanostructures

Analytical grade $FeSO_4.7H_2O$ (Merck), NaOH (Merck), starch (Merck), and $Cu(NO_3)_2.3H_2O$ were used for the synthesis of starch functionalized $Fe_3O_4/Cu_2O$ photocatalysts. The first step was to prepare SMNPs (as in the previous section). After that, re-dispersed SMNPs (60 mg of in 60 mL double distilled water) was mixed with 25 mL of 0.01 M $Cu(NO_3)_2.3H_2O$ (Merck) aqueous solution. This suspension was agitated at 60 $^0$C for 24 hours to achieve adsorption equilibrium. Further, an appropriate amount of 0.5 M glucose (Merck) solution was added to the suspension, followed by dropwise addition of 50 mL of 1 M NaOH with constant heating at 80$^0$C and stirring. The precipitate was then separated by magnetic decantation method and washed several times with double distilled water until the washings turned neutral and dried (at 40$^o$C) in a hot air oven. The symbol CF denotes the resulting nanocomposite.

### 2.3.3 Synthesis of starch functionalized α-FeOOH/β-FeOOH nanocomposites

Analytical grade anhydrous $FeCl_3$ (Merck), starch (Merck), NaOH (Merck) were used without further purification. The aqueous solution of an appropriate amount of anhydrous $FeCl_3$ (Merck) was mixed with freshly prepared 2wt% aqueous starch (Merck) solution. The mixed solution was heated at 80-90$^o$C with mechanical stirring for 15 minutes. Subsequently, an appropriate amount of 32 M NaOH was added to the above mixture in a dropwise manner. After complete addition, the whole reaction mixture was maintained at the same temperature for two more hours to ensure complete precipitation. The precipitate was repeatedly washed with deionized water to remove excess NaOH and make it neutral. In the final step, the precipitate was dried in a hot air oven. The label S2 represented the resulting nanocomposite. Non-functionalized iron oxyhydroxide nanocomposite was also prepared and labeled as S1.

### 2.3.4 Synthesis of starch functionalized α-FeOOH/β-FeOOH/$Cu_2O$ nanostructures

Chemicals used in the synthesis of starch functionalized α-FeOOH/β-FeOOH /$Cu_2O$ nanostructures were of analytical grade. Starch functionalized FeOOH nanoparticles (S2) were prepared as in section 2.3.3. The synthesized S2 nanocomposite (60 mg) was re-dispersed into double distilled water and added to 25 mL of 0.01 M $Cu(NO_3)_2.3H_2O$. The suspension was kept for 24 hours at 60 $^0$C to achieve adsorption equilibrium. Next, the suspension was added in a dropwise manner to 50 mL of 0.15 M NaOH with constant heating and stirring at 60 $^o$C. Total precipitation required heating of the obtained reaction mixture at 60 $^o$C with stirring for two more hours. The obtained precipitate was then washed several times with double distilled water and dried at 50$^o$C in a hot air oven. CSP denotes the prepared powder sample.

## 2.4 Photocatalytic Experiment

### 2.4.1 Design of photocatalytic chamber

The photocatalytic chamber is a four-sided cubical box. A 7W cool white LED is fixed on each wall of the chamber. Besides this, a cool white LED of power 14W (Philips) is also fixed on the ceiling of the box. Overall, the reaction mixture in a four-sided quartz cuvette was irradiated by approximately 0.1470 watts/cm$^2$ power. The solar power meter TM-206 was used to measure the power of irradiation. The temperature inside the photocatalysis chamber was constant at 303 K throughout the reaction.

### 2.4.2 Photocatalytic production of $H_2O_2$ on starch functionalized $Fe_3O_4$/Ag/$Ag_2O$ nanostructures

Exactly 4mL of water was added to 400 µL of re-dispersed photocatalyst (3 mg in 10 mL water) suspension. The suspension's pH was adjusted to 3 by suitable addition of 0.1 M HCl.

The reaction mixture was kept in the photocatalytic chamber under cool white LED irradiation for 1 hour. The photocatalyst was then magnetically separated from the reaction mixture. The $H_2O_2$ generated in the remaining liquid was determined by redox titration against 0.2 mM $KMnO_4$ acidified by 1 M $H_2SO_4$. The appearance of light pink color marked the endpoint.

### 2.4.3 Photo-Fenton PNP degradation

Precisely, 176μM of PNP was taken in a standard quartz cuvette of 1 cm path length. Next, this solution's pH was adjusted to 3 (acidic) by using 0.1 N HCl or 0.1 N NaOH. An appropriate amount of catalyst was added, and the obtained suspension was then allowed to stand (for 60 minutes) until adsorption equilibrium. In the subsequent step, 100μL of 50 mM $H_2O_2$ solution was added to catalyst suspension. Absorption spectrums were recorded at regular intervals. A blank reaction (in the absence of a catalyst) was also conducted and monitored by UV-vis spectrophotometer at fixed time intervals.

### 2.4.4 Photo-Fenton MO degradation

An acidic solution of 140 μM MO was taken in a standard quartz cuvette of 1 cm path length. The MO solution's pH was adjusted to 3 by using 0.1 N HCl or 0.1 N NaOH. Next, an appropriate amount of catalyst was added, and the suspension allowed to stand until adsorption (for 60 minutes) equilibrium. After that, 100μL of 50 mM $H_2O_2$ solution was added to the reaction mixture. The absorption spectrums were recorded at regular time intervals.

## 2.5 Techniques used for photocatalysts characterization

This section discusses different techniques used to characterize various features of photocatalysts prepared in this thesis. The characterization techniques used were UV-visible

spectroscopy (UV-Vis), UV diffuse reflectance spectroscopy (UV-DRS), X-ray diffraction (XRD), Fourier transform infrared spectroscopy (FTIR), Transmission electron microscopy (TEM), Magnetic property measurement system (MPMS), X-ray photoelectron spectroscopy (XPS) and Electrochemical impedance spectroscopy. XRD was used to identify the phases formed and crystallite sizes. FTIR analysis helped to identify the different functional groups present on the surface of nanoparticles due to functionalization. Nanostructure imaging by TEM was necessary for determining the shape and size of the prepared particulates. XPS analysis of the nanostructure surface identified the chemical species present. The photocatalyst bandgap was found by Tauc plot analysis of the UV-DRS (solid-state) spectroscopy data. The electrochemical workstation/ analyzer was utilized to investigate the prepared nanostructures' flat band potential and band edges. UV-Vis spectroscopy was used to investigate the kinetics of photocatalytic degradation of PNP and MO. The magnetic properties of the prepared powder samples were analyzed with MPMS.

### 2.5.1 UV-Visible spectrophotometer

The UV-visible absorption spectroscopy measurements were performed on an Agilent Cary 60 spectrophotometer (Figure 2.1). There are two light sources in this spectrophotometer. A deuterium or hydrogen discharge tube covers the UV region (200-370 nm) and a second tungsten lamp scans the visible region (325-770 nm). All samples in the present thesis were appropriately diluted and taken in a quartz cuvette of 1 cm path length for UV-visible measurements.

**Principle**

Absorption of ultraviolet or visible light (of frequency ($\upsilon$) or wavelength ($\lambda$)) results in the electronic transitions from lower to the higher energy levels of the molecule. UV-

visible irradiation can excite an electron from non-bonding (n), or a π-orbital, to an antibonding π–orbital (π*) or antibonding σ-orbital (σ*). As per Beer-Lambert's law, the incident radiation absorbed is directly proportional to the concentration of absorbing molecules in the solution and the length of path it has to travel through the absorbing medium. Secondly, the fraction of incident radiation absorbed by a solute in a transparent solvent is independent of incident light intensity. Equation 2.1 expresses this law.

$$log \frac{I_0}{I} = A = \varepsilon cl \qquad (2.1)$$

Here $I_0$ is the intensity of incident light, $I$ is the intensity of transmitted light, $A$ is absorbance, $\varepsilon$ is molar extinction coefficient or molar absorptivity (a function of the frequency of light), $c$ is the concentration of solute, and $l$ is the cell path length (1cm).

Hence, the peak intensity depends upon the number of molecules that absorb light of a given wavelength. The adsorptive concentration, reactants utilized, and products formed can be determined in-situ in a dilute solution or reaction mixture by UV-vis spectroscopy.

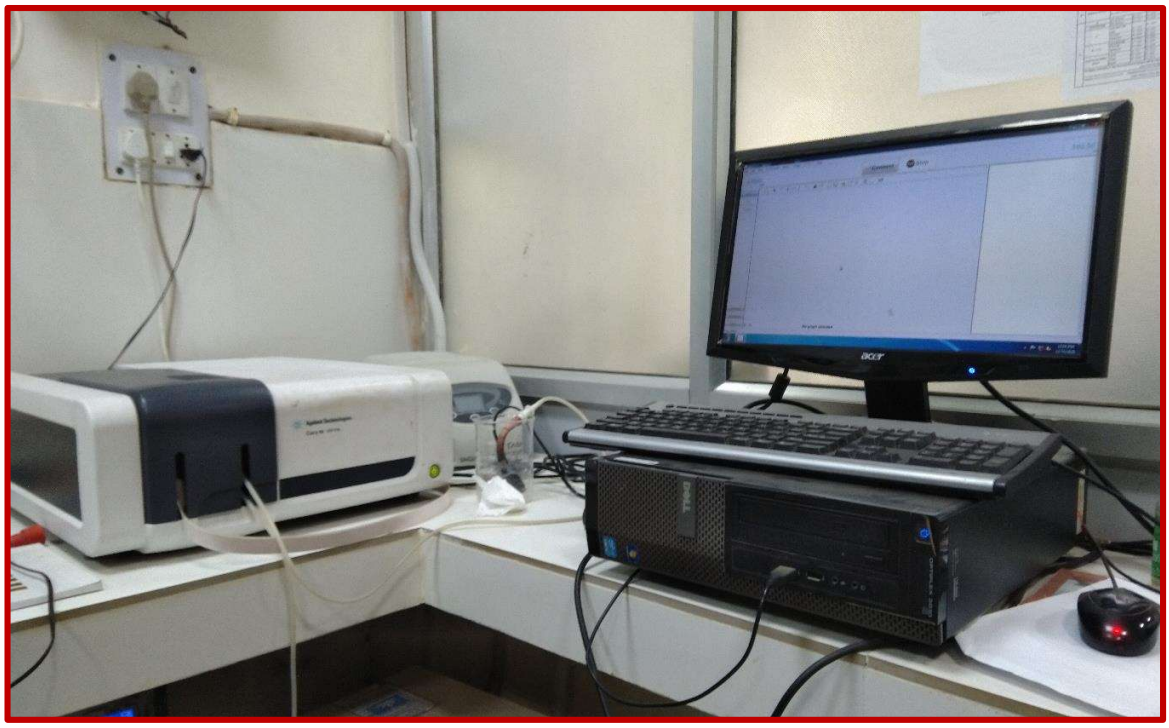

**Figure 2.1** UV-Visible spectrophotometer (Agilent Cary 60).

### 2.5.2 UV-Vis diffuse reflectance spectroscopy (UV- DRS)

Solid-state UV-visible measurements were done on the Shimadzu Pharmaspec UV-1700 model in the 200−800 nm spectral range. The solid-state spectrum was used to derive the optical bandgap of the prepared nanostructure.

**Working principle**

The bandgap energy was determined from Tauc Plot using optical absorption spectra. The Tauc plots were constructed using the following relation.

$$\alpha = \left(\frac{\beta}{h\nu}\right)(h\nu - E_g)^n \quad \text{or} \quad (\alpha h\upsilon)^{1/n} = (h\nu - E_g) \qquad (2.2)$$

Here, α represents the molar absorption coefficient, υ denotes the frequency of light, and $E_g$ is the material bandgap. The intercept of the linear part of the plot of $(\alpha h\upsilon)^{1/n}$ versus hυ on the abscissa gives the optical band gap ($E_g$) energy of photocatalyst. The exponent n

determines the nature of the optical transition. For indirect transition, the value of n is 2, while n is equal to ½ for a direct transition.

### 2.5.3 X-ray Diffraction (XRD)

The XRD spectra of nanostructures prepared in this thesis were recorded on the Mini Flex 600 (Rigaku, Tokyo, Japan) instrument displayed in Figure 2.2. Primarily the instrument consists of an X-ray generation source, optics, goniometer, and detector. An optional graphite monochromator, Soller slit (5.0° or 2.5°), and fixed scattering slit make up its optical setup. It has a 150 nm radius vertical goniometer with an accuracy of ± 0.02°. NaI scintillator and high-speed silicon strip are the detectors in Mini Flex 600. Tube voltage of 40 kV and 15 mA current were used in the running of the XRD. All the XRD measurements in this thesis used Cu-$K_\alpha$ radiation with wavelength 1.54059 Å. For sample analysis, a thin layer of powdered nanomaterial sample was placed in a goniometer rotating at the rate of $1^0$ per minute with a step size of 0.02.


**Figure 2.2** XRD diffractometer (Mini Flex 600).

**Principle**

The X-ray powder diffraction technique can identify the phases in a crystalline material. It can also determine the crystallite sizes and the unit cell dimensions of the identified crystal phases. The technique utilizes the constructive interference of monochromatic X-rays diffracted by the crystal planes of a sample. The interaction of incident X-ray with the crystalline material powder sample produces constructive interference (and a diffracted ray) when conditions satisfy Bragg's law.

$$n\lambda = 2dsin\theta \qquad (2.3)$$

Here n is the order of reflection, i.e., 1, 2, 3,……, λ represents the wavelength of incident radiation, d is the inter-planar spacing, and θ is Bragg angle.

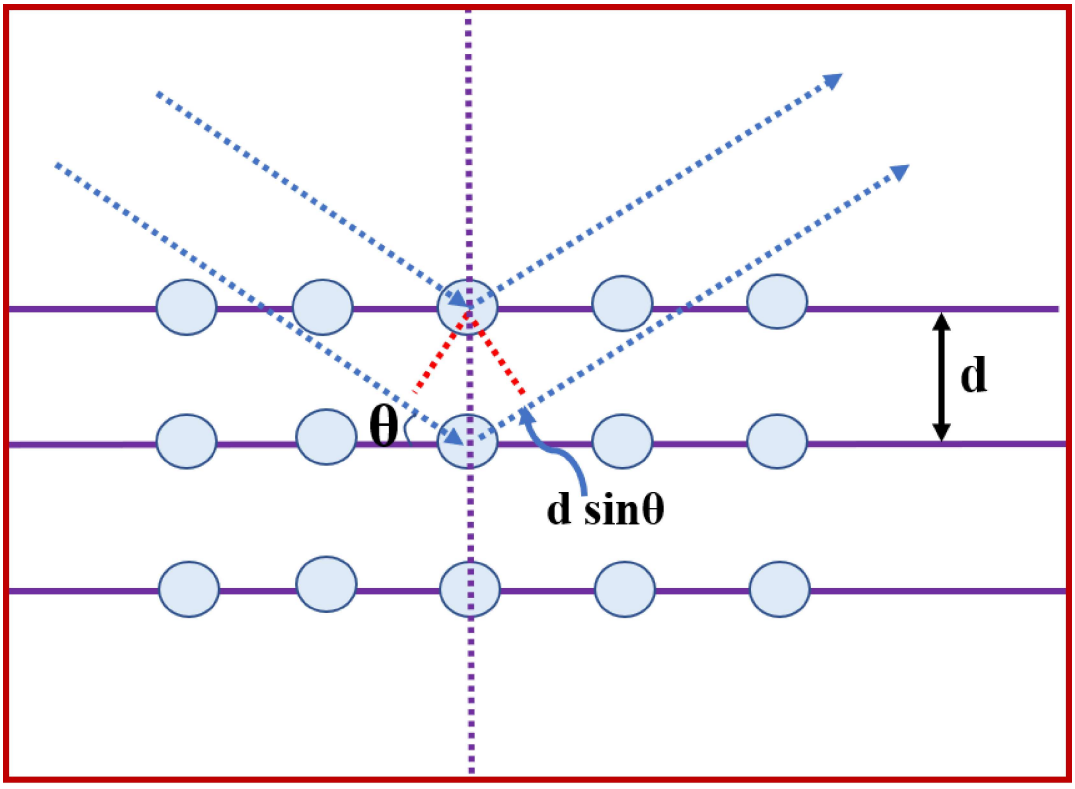


**Figure 2.3** Schematic explaining diffraction occurring as per Bragg's law.

Peak broadening in XRD patterns can be used to find average crystallite size (or coherently scattered domain size) in the material. Such broadening is quantified by the full width half maximum (FWHM) of a peak from the diffraction pattern. Scherrer's formula was used to calculate the average crystallite size.

$$D = \frac{k\lambda}{\beta cos\theta} \qquad (2.4)$$

In this expression D is the coherently scattered domain size, k represents dimensionless constant (≈0.9), λ is the wavelength, β indicates instrument corrected FWHM in radian, and θ is diffraction angle. [Cullity *et al.* (2001)].

### 2.5.4 Fourier Transform Infrared Spectroscopy (FT-IR)

Fourier transform-Infrared spectroscopic measurements were conducted on Varian 3100 FT-IR spectrometer. FT-IR spectroscopic analysis was carried out by mixing nanomaterial powder sample with KBr in agate pestle and mortar followed by palletization. FT-IR spectra were recorded between spectral range 4000 and 400 $cm^{-1}$, with a resolution of 0.09 $cm^{-1}$.

**Principle**

IR is a non-destructive technique for functional group analysis. FTIR is a useful technique for analyzing organic materials and certain inorganic materials as it provides specific information about the vibration and rotation of the chemical bonding and molecular structures. Various molecular vibrational modes such as bond stretching or bending in molecules can be excited from lower vibrational energy states to higher vibrational states by absorbing IR radiations. All vibrational modes of bonds in a molecule are not capable of absorbing IR energy. Only those vibrational modes that are accompanied by a change in the molecules' dipole moment result in active infrared transitions. An infrared spectrum

represents a fingerprint of a sample with absorption peaks, which correspond to the frequencies of vibrations between the bonds of the atoms making up the material. Each material has a unique combination of atoms, thus produces a characteristic infrared spectrum. Therefore, every different kind of material could be easily identified by infrared spectroscopy (qualitative analysis).

### 2.5.5 Transmission electron microscopy (TEM)

FEI Technai-20 $G^2$ at an operating voltage of 200 keV was used to record TEM micrographs of prepared nanostructures (Figure 2.4). The powdered samples were re-dispersed in ethanol to a dilution of about ten times required for sample preparation for UV-Vis absorption measurement. The re-dispersed sol was sonicated for 30 min in a water bath. After that, one drop of this sonicated sample was dropped on a carbon-coated Cu grid (400 mesh size). The CF and CSP samples were prepared on a carbon-coated Ni grid of 200 mesh size. The grid was dried for 24 hours in a vacuum oven at 50°C (at 550mmHg pressure) before microscopic investigations.

TEM images are used to recognize the morphologies of particles found in the sample. The average particle size and size distribution are also obtained by proper statistical sampling. Different phases in nanocomposites can be identified from corresponding high-resolution TEM (HR-TEM) images.

**Principle**

The TEM uses an electron beam instead of light. The electron beam wavelength is much smaller than that of light, and hence, TEM images are of much higher resolution than an optical microscope. A beam of high energy electrons is focused onto a sample in this microscopy, causing an enlarged version to appear on a fluorescent screen or photographic

film layer. TEM is capable of giving information both in real as well as in reciprocal space. Therefore, it provides morphological and structural information about the specimen. Its energy dispersive spectroscopy (EDS) can reveal its elemental composition present in the material. Moreover, it gives a better understanding, especially for atomic resolution real spacing images of material at the nanoscale [Wang *et al*. (2000)]. The image formed is magnified further to be detected by the sensor, such as a CCD camera.

**Figure 2.4** Transmission electron microscopy (FEI Technai-20 $G^2$).

The TEM instrument consists of three parts moving from top to bottom: (1) an electron gun, (2) an image producing system, (3) an image recording system. The electron gun is a cathode made up of tungsten or LaB6, which produces an electron beam [Egorton *et al.* (2005)]. The electron beam, transmitted from the cathode, passes through the columnar aperture (hole) to the anode at high voltage with constant energy, which is efficient for focusing the specimen on producing an accurately defined image. It also has the condenser lens system, which works to focus the electron beam on the sample by controlling the electron

gun's energy intensity and column hole. There are two condenser lenses to converge the beam of electrons to the specimen to produce an image. With strong magnification, the first lens produces a smaller image of the sample, and the second condenser lens directs the image to the objectives. The image size may be varied by controlling the first lens [Rose *et al.* (2008)]. Computerized images are stored in a TIFF or JPEG format and analyzed.

### 2.5.6 Magnetic property measurement system (MPMS)

The magnetic property of nanocomposites was investigated using SQUID Based Magnetometer (Quantum Design Inc.). The instrument tracks the change in magnetic flux. It also detects and measures the magnetic moment of the sample.

**Principle**

The SQUID magnetometers are very sensitive. It consists of two semiconductors separated by thin insulating layers to form two parallel Josephson junctions. It allows fully automated measurement of the specimen's magnetization as a function of magnetic field or temperature [Buchner *et al.* (2018)]. It does not directly measure the magnetic moment. SQUIDs can only detect magnetic flux $\Phi=\int B\cdot dA$, where B is magnetic flux density, and A represents the SQUID loop area. It also measures the current exited in the superconducting loop (called a flux transformer) due to a change in the magnetic flux. According to Brian David Josephson (1962), the electrical current density through a weak electric contact between two superconductors depends on the phase difference $\Delta\varphi$ of the two superconducting wave functions [Drung *et al.* (2007)]. Moreover, the time derivative of $\Delta\varphi$ is correlated with the voltage across this weak contact. In a superconducting ring with one (so-called rf SQUID) or two (dc SQUID) weak contacts, $\Delta\varphi$ is additionally influenced by the magnetic flux $\Phi$ through this ring.

### 2.5.7 X-ray photoelectron spectroscopy (XPS)

XPS was carried out on ESCA M-Probe (Al Kα rays λ = 8.33 Å) and Thermo fisher scientific make K-Alpha (Figure 2.5). Survey scans were performed with a detector pass energy of 158.9 eV, and the high-resolution spectra were recorded with a pass energy of 22.9 eV. All spectra were referenced to adventitious carbon signal at 284.8 eV with Casa XPS software from Casa Software Ltd. The parameter DS (0.0001,400) line shape for elemental Ag metal peaks and GL (30) line shape were used for fitting all other peaks


**Figure 2.5** X-ray photoelectron spectroscopy (Thermo fisher scientific make K-Alpha).

**Principle**

XPS is a quantitative technique for analyzing the surface chemistry of a material. XPS can measure the composition, empirical formula, chemical state, and electronic state of elements on a material's surface. XPS is based on the photoemission process. Figure 2.6 shows the schematic representation of the photoemission process. When an atom or molecule absorbs an X-ray photon, an electron gets ejected. The kinetic energy (KE) of the electron depends upon the photon energy (hν) and the binding energy (BE) of the electron (i.e., the

energy required to remove the electron from the surface). By measuring the kinetic energies of the emitted electrons, it is possible to identify elements at the material's surface, their chemical states, and their binding energies. Thus, XPS spectrum measurement involves irradiating a solid surface with a beam of X-rays, and at the same time, determining the kinetic energies of electrons emitted from the materials' surface. Hence, a photoelectron spectrum consists of counting the electrons ejected over a range of kinetic energies.

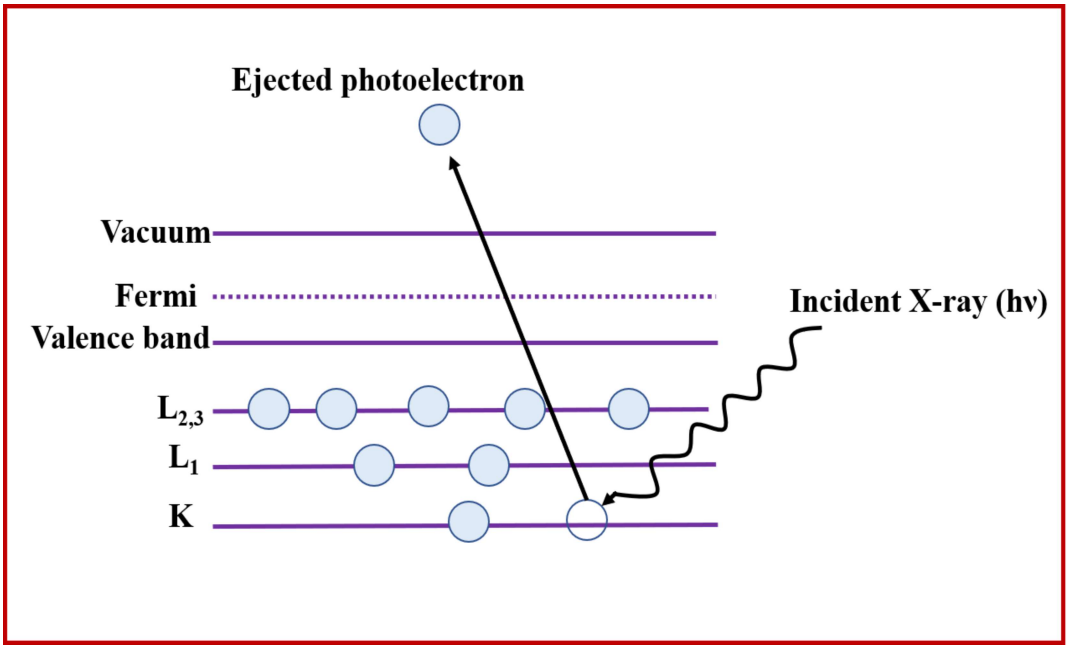


**Figure 2.6** Schematic representation of the photoemission process.

### 2.5.8 Electrochemical workstation/analyzer

The electrochemical analysis of the semiconductor heterostructures was performed on CH instrument model CHI-7044. In this thesis, the Mott-Schottky (MS) plot and Nyquist plot were constructed using the electrochemical analysis data. The MS plot gives information about flat band potentials. If one assumes that the gap between the flat band potential and the lower edge of CB is negligible for an n-type semiconductor, then the CB potential of the n-type semiconductor becomes roughly equal to its flat band potential. Similarly, if it is

assumed that the gap between the flat band potential and the top edge of the VB is negligible for a p-type semiconductor, then the VB potential of the p-type semiconductor becomes equal to its flat band potential. In this way, one can determine the CB and VB band edge positions of a semiconductor. The MS plot slope gives information about the semiconductor material type (p- or n-). The Nyquist plots of electrochemical impedance spectroscopy (EIS) provide the electron transfer kinetics of the catalysts.

**Principle**

An electrochemical workstation has a potentiostat with relevant control software on one end and the electrochemical cell setup. A potentiostat is an electronic instrument that controls the voltage difference between a working electrode and a reference electrode in an electrochemical cell. It injects current into the cell through an Auxiliary or Counter electrode to control voltage difference. It also measures the current flow between the working and counter electrode. The three electrodes in the electrochemical cell setup are the working, the reference, and the counter electrodes. These electrodes are immersed in an electrolyte. The control of potential and current measurement takes place at the working electrode. The working electrode is made of inert materials such as gold, platinum, or glassy carbon and measures the current flow. The reference electrode measures the working electrode potential and has a constant electrochemical potential as long as no current flows through it. The most common reference electrodes are the saturated calomel electrode (SCE) and the silver/silver chloride (Ag/AgCl) electrodes. The third Counter or the Auxiliary electrode is a conductor that completes the cell circuit. The Counter Electrode is generally an inert conductor like platinum or graphite. It is also regarded as another part of the working electrode material. The current that flows into the solution via the working electrode leaves the solution via the counter electrode.